Sediment erosion in flexible canopies by vortex impact

Qianhui Li and Christoph H. Bruecker

School of Mathematics, Computer Science and Engineering. City, University of London, UK

Abstract

A model experiment with a vortex impacting a flexible canopy filled with a thin homogeneous bed of particles is presented. Flexibility of the filaments increases the efficiency of resuspension by the amount it allows the effective canopy-height to reduce due to the reconfiguration of the flexible structures. Scaling of the results with the effective canopy height leads to a collapse of the observed resuspension in the history of several successive impacts. It is further shown that preferential pathways in the canopy play a large role in resuspension. When comparing a hexagonal arrangement to a random arrangement of the filaments at the same average porosity, one needs to double the amount of impacts to achieve the same average resuspension. Hence, it is concluded that the random path of the particles around the filaments is affected in a non-linear manner by the local resistance. Regions of locally sparse arrangements of the filaments cannot balance the trapping effect of particles within regions of dense arrangement in their travel history. Flexibility of the filaments again proves a better resuspension under such conditions.

Keywords: resuspension, vortex ring, flexible canopies

1. Introduction

Resuspension and erosion of particles by shearing flow widely exist in a series of natural phenomena such as sediment transport in rivers and dune formation in the desert. It also plays an important role in both industrial and environmental processes to control particle transport (Ouriemi et al. 2007). For example, it requires effective transportation of the particulate matter such as granular flow in food or pharmaceutical process via pipeline systems, whereas there is a requirement to prevent sediment resuspension in sewage sedimentation tanks and dust loss from soils which reduces soil fertility (Bethke and Dalziel 2012). Therefore, it is of great importance to understand the physical mechanism of sediment transport and redistribution to achieve effective control of it. Usually the sediment is nested within larger canopy layers such as the soil in crop fields, the sand layer in sea-grass, or canopies of larger scales as e.g. in forests. A recent review of turbulent flows over vegetation was given by Nepf (Nepf 2012) showing how fluid instabilities at the interface of the fluid-canopy layer modify the transfer of mass and moment within the canopy. A strong interaction is observed if the canopy is flexible and the elements in the canopy undergo considerable deformation, summarized in the review of wind over flexible canopies given by De Langre (De Langre 2008). However, as mentioned in (Bethke and Dalziel 2012) the Reynolds number of the corresponding fluid flows is often high, which makes the understanding of particle transport underlying on the turbulent interaction of the fluid flow with the complex dynamics of the particles and the canopy structures difficult. Thus, a generally valid macroscopic model of particle transport in such configurations does not exist to date.

Recent numerical simulations of turbulent flow over canopies are able to include the elastic response of the structures. However, most of these studies are limited to low turbulent Reynolds numbers and for the linear-elastic regime. Bottaro (Bottaro 2019) was able to use multiscale homogenization for canopies consisting of periodic or quasi-periodic microstructures, avoiding the numerical resolution of small details such as the flow around individual elements of the canopy e.g. filaments. He considered the flow above solid surfaces with microscopic protrusions, with the wall roughness either rigid or linearly elastic and developed the underlying equations. This is relevant to the interaction of turbulent flows with filamentous walls, which are of growing interest for flow control along engineered aerodynamic / hydrodynamic surfaces (Bottaro 2019). The work also summarizes the recent developments in numerical simulations of canopy flows. The simulation most relevant to this study was done by Sundin and Bagheri (Sundin and Bagheri 2019), who simulated the interaction between hairy surfaces and turbulent flows in a turbulent channel flow configuration. Their work was inspired by the experimental observation of streak stabilization in turbulent boundary flows over arrays of flexible filaments (Brücker 2011). This two-way coupled interaction on different time-scales with the fluid flow and the mechanical system is difficult to achieve in numerical simulations as argued by Bottaro (Bottaro 2019). The pointwise approach used by Sundin & Bagheri (Sundin and Bagheri 2019) may become difficult for dense coatings when the fluid simulation through the deforming filaments requires a more microscopic description. Furthermore, additional simulation of the transport of particles within the canopy may be out of reach at the current computational power of supercomputers. Therefore, further insight may be gained in laboratory experiments under controlled and repeatable conditions.

The experiments presented here address this need by studying the vortex-induced resuspension of particles within a canopy of slender flexible filaments, aiming to contribute to the growing interest for flow control along engineered aerodynamic / hydrodynamic surfaces built of such filamenteous layers. In practical situations, the performance of such surfaces is often diminished by the accumulation of dust particles or other particulate matter in the layer. For effective two-way coupled interaction of the turbulent near-wall flow with the filaments, their typical length was chosen in the previous studies of order of the characteristic scale of the coherent vortex structures in turbulent boundary layers near the wall, the so called hairpin vortices (Brücker 2011, Sundin and Bagheri 2019). Instead of addressing the full range of turbulent scales, the present study follows the strategy of using a single vortex ring as a prototype of this elementary hairpin vortex structure, impacting with the canopy in a head-on collision. Such a prototypical model was first used by Sutherland (Sutherland 1967) for the study of resuspension in a sediment layer on a flat plate. We have set the Reynolds-number of the vortex ring to Re=800, which is comparable to that of a hairpin vortex near the wall (Bandyopadhyay and Balasubramanian 1995). The canopy height is chosen equivalent to the vortex-core radius and the canopy properties (filament size, spacing, Cauchy-number) are leaned upon the recent numerical study of Sundin and Bagheri (Sundin and Bagheri 2019). They have studied numerically a turbulent channel flow at similar local ratio of the smallest vortex size to canopy height, and, as our canopy properties are similar, we might observe some similar features of the interaction. However, with the wall-normal impact of the vortex ring we are largely simplifying this turbulent interaction, mainly for practical, experimental reasons. The quasi-cyclic occurrence of coherent structures in turbulent flows and their penetration into the canopy is simulated herein with successive shoots of the vortex ring at the same location onto the canopy. This laboratory experiment with a laminar vortex-ring is therefore limited in relevance and conclusions to the specific conditions of the canopy, the vortex structure and the particles used herein rather holds as a benchmark test for numerical simulations under well-defined and repeatable boundary conditions. That those benchmark tests for engineered canopies are much needed and welcome to this community was recently highlighted by (Bottaro 2019) in his review article.

The present study might have some relevance in nature for Archerfish, as they are known for shooting jets underwater towards the sand floor to expose hidden prey or food (Dewenter et al. 2017). Therein, the fish use different angles and distances from the sand layer for generating a wash-out effect with formation of a sand cloud. The authors argue that the fish adapt their shots to different ground material when the fish explored for buried prey items; when food is buried in substrate that consists of large particles, the fish use a short pulse, but they use a longer one when the substrate is more fine-grained (Dewenter et al. 2017). The work differs from previous studies on vortex rings impacting with sand layers under water (Munro, Bethke, and Dalziel 2009, Bethke and Dalziel 2012) as the base herein is not a smooth flat wall but is formed as a canopy composed of slender filaments. The sediment layer consists of near-spherical sand particles with a mean diameter of 500 µm and relative density of 1.36, which are initially homogeneous distributed in a horizontal layer within the forest of vertical posts of diameter 1mm and inter-spacing of 4mm (the canopy). A series of repeated vortex impacts is carried out while the deformation of the sand layer is recorded after each impact under otherwise constant parameters of vortex size, strength, velocity and travel path in a quiescent fluid. In one experiment, the posts of the canopy are rigid, in another experiment the posts are flexible and allowed to bend with the penetrating vortex. Furthermore, the arrangement of the posts is varied to study the effect of anisotropy of resistance and drag within the canopy. We compared a hexagonal grid of posts to a random grid at the same average porosity. The results are examined in terms of the effective resuspension, measured from the attenuation of light through the bed, while velocity field measurements complement the flow structure above the canopy layer during impact.

2. Experimental set-up and conditions

The experimental setup is shown in Fig. 1 following our previous study on the vortex interaction with a rough wall (Li and Bruecker 2018). A piston-cylinder nozzle (nozzle outlet diameter 30mm) is installed at the top of the liquid tank to generate the vortex ring with a radius of $R = D/2$ = 22 mm at an initial travelling speed of U_0 = 400 mm/s. The radius of the vortex core is measured to R_c = 5 mm. The calculated ring circulation follows $\Gamma_0 = \int \omega_\theta drdz$ and yields 180 cm²/s, resulting in a circulation-based Reynolds number $Re_\Gamma = \Gamma_0/\nu$ = 800. The time is made non-dimensional in the form $t^* = t\Gamma_0/R^2$ (it multiplies 38/s with the physical time in seconds) and starts at zero when the roll-up process of the shear layer at the nozzle is finished. At 20 cm downstream from the nozzle exit, a transparent canopy layer with 2 mm thick disc-shaped base adhered on a glass plate is placed horizontally in the tank, below which a surface mirror is arranged 45° from the horizon and faces to the camera. As the vortex ring travels downstream, it impacts in a head-on collision with the canopy layer, which is formed by a forest of slender cylindrical posts. Within the canopy, a homogeneous layer of sand particles is placed. We observe the erosion of such particle layer during the impact of the vortex ring when the posts have different flexibility. The non-dimensional time of impact in the present study is defined at the moment when the free travelling vortex passes the origin of the coordinate system at t_0^* = 15. An additional time scale $T = t^* - t_0^*$ is defined to compare the different experiments after impact.

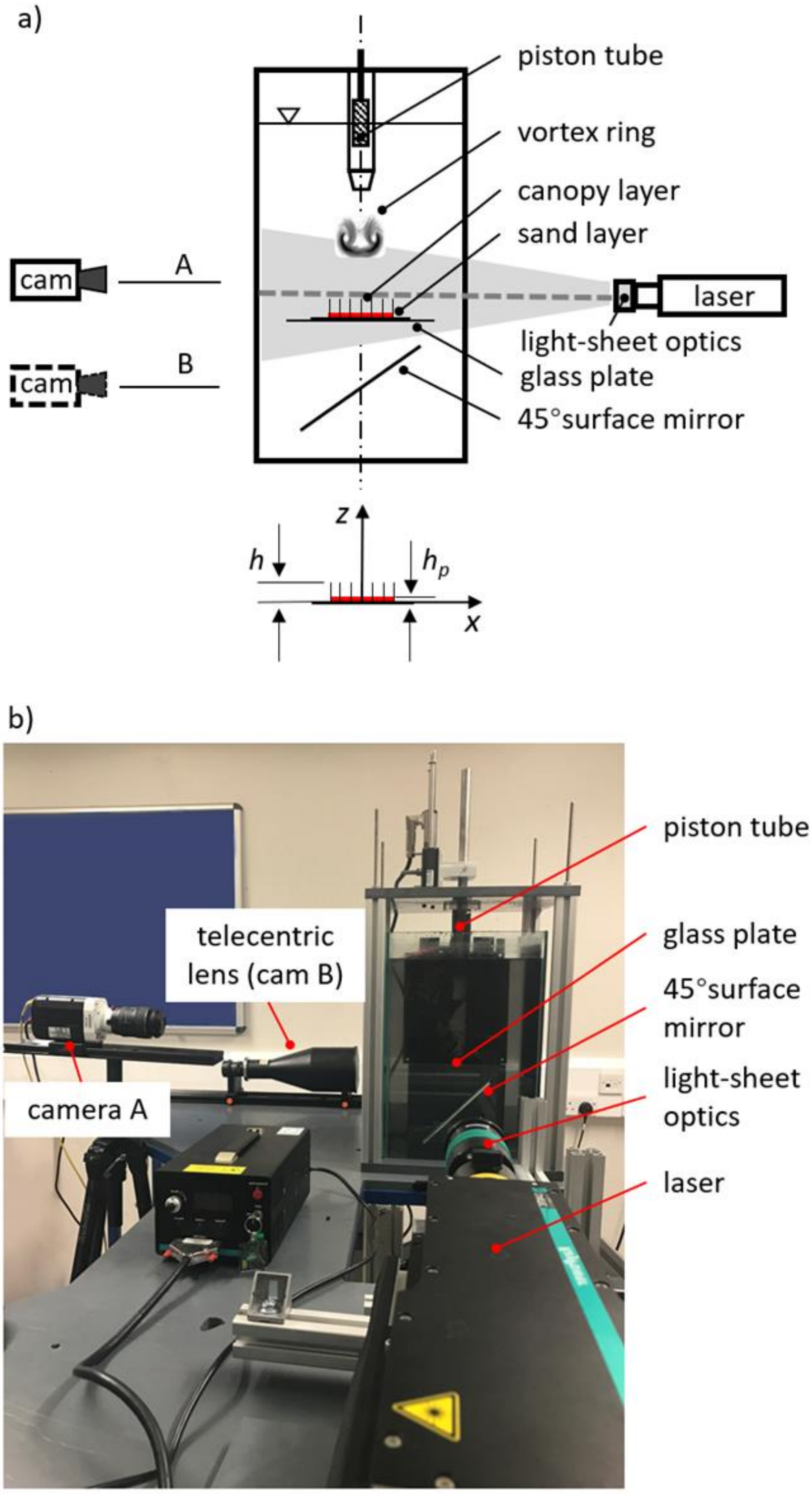

Fig. 1. Schematic of the experimental setup a) and picture of the actual flow rig b). The sketch in a) shows the laser rotated into the paper plane. Camera configuration A is used with a vertical light-sheet to record the flow field in the vertical *x-z* plane; configuration B is used to record the flow field in the radial *x-y* plane above the canopy layer. Similarly, camera configuration A measures the displacement of the flexible canopy filaments in the vertical x-z plane while configuration B is used to record the displacement of flexible canopies' tips in the radial x-y plane. Finally, for sand layer erosion measurements, the camera configuration B measures the intensity distribution of the light coming

from the top and travelling through the bed within the transparent canopy and base (glass plate), viewed by the camera through a 45° surface mirror. The coordinate origin is at the centre of the axis of the vortex ring on the surface of the glass plate.

Two canopy layers with the same dimension and structure but different flexibility are comparatively investigated. One type is composed of rigid filaments (rigid cylindrical posts of diameter *d=1mm* and height *h=10mm*) and the other is composed of flexible filaments of the same cylindrical shape. As mentioned in the introduction, the height of the canopy layer is chosen equal to the characteristic size of the vortex core ($2R_c$ = 10 mm). The canopy layer with flexible filaments is cast from transparent silicone (Poly-Di-methyl-Siloxane PDMS, Wacker Silicones) (Young's modulus $E \approx$ 1.24 MPa), poured into a rigid mold which is perforated by laser drilling, see the method described in (Schmitz, Brücker, and Jacobs 2005). After curing, the cast with the filament is peeled off. The rigid one is made by 3D printing with transparent resin. The working liquid is a water- glycerol mixture (70/30 % by mass, density $\rho = 1.18\ g/cm^3$, kinematic viscosity $\nu = 22.5 \times 10^{-6} m^2/s$) which matches the refractive index of the silicone material (*n*=1.4). Fig. 2 shows the dimension and structure of the canopy layer and the particle layer. The slender posts are distributed in a regular grid (x_i, y_i) with a hexagonal pattern or alternatively in a random pattern, forming a porous canopy layer with an open interface at the top and closed interface at the wall. The average porosity of this layer is calculated by the ratio of void volume to total volume, yielding ϵ=0.94. With the given conditions, our filamentous canopy structure is of similar structure as the filamentous wall used in the numerical study of Sundin and Bagheri (Sundin and Bagheri 2019) (in theirs *h*/*d*=5, *s*/*d*=2 and 4, in our study *h*/*d*=10, *s*/*d*=4). Furthermore, with the given material parameter of the silicone we reach the same filament Cauchy number of Q^* $\sim$ 1, see below. Finally, the canopy height in their turbulent flow simulations is chosen such that it compares to the scales of the smallest coherent vortex structures (hairpin vortices) near the wall. Therefore, our study with the vortex ring is at a similar ratio of canopy height to characteristic vortex size, which let us assume stronger interaction with the bed similar as observed in their study.

Sand particles ($\rho_p = 1.602\ \mathrm{g/cm^3}$ (dry)) with the average size of $d_P = 500$ µm are uniformly distributed within the canopy layer in a loosely-packed arrangement. Great care was taken to achieve a flat horizontal layer of the sediment with constant thickness prior to the impact experiments.

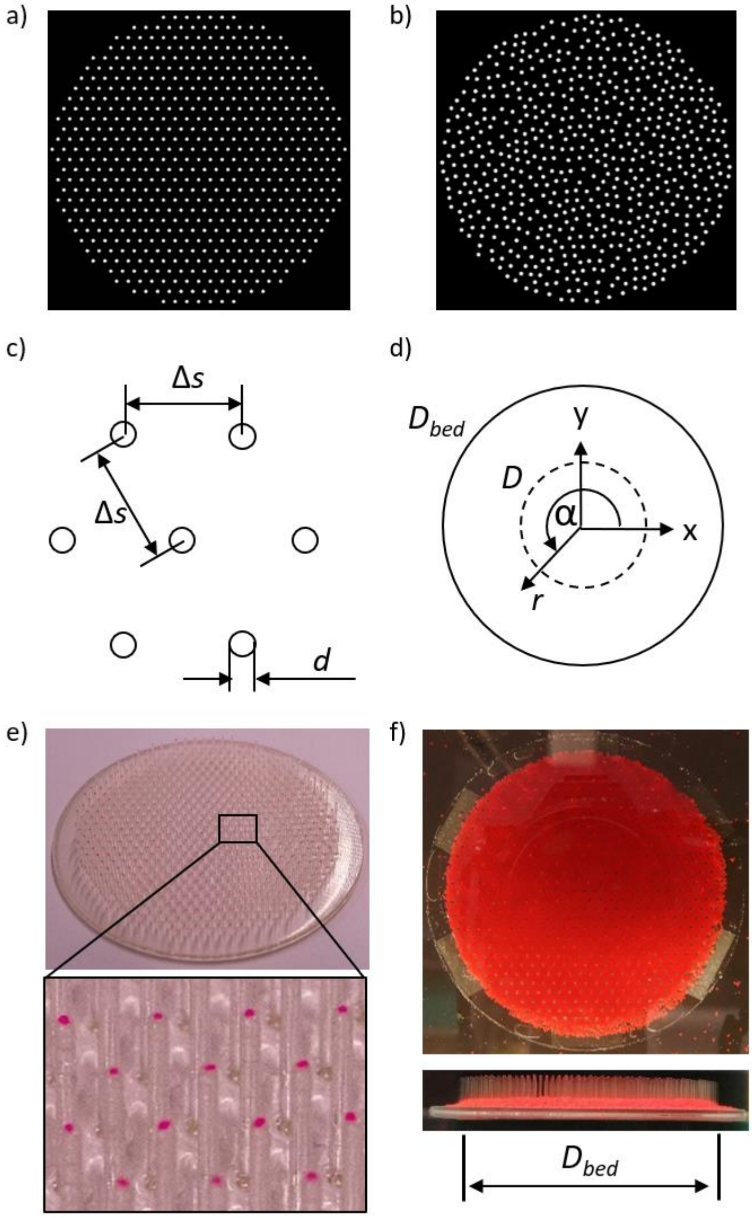

Fig. 2. Dimension and structure of the canopy layer. a) Slender filaments arranged in a hexagonal lattice and b) in randomly distribution, with the same number density. c) Filaments with constant diameter d = 1 mm are spaced in the hexagonal grid as shown with Δs = 4 mm. d) Coordinate systems in the bed with diameter D_{bed}=100 mm, for comparison the torus of the vortex ring with diameter D=44 mm is indicated as a dashed circle. e) Picture of the canopy layer with filaments (initial height h=10mm) protruding out. The tips of the canopy layer are fluorescent-labeled by fluorescent dye. f) Bottom and side view of the sand layer uniformly distributed within the canopy.

Following the discussion of flexible wall-mounted filaments in flow (Brücker, Bauer, and Chaves 2007), (Sundin and Bagheri 2019), the mechanical system of the filament can be described in first approximation as a clamped cantilever beam and is described by the Euler-Bernoulli equation

$$EI\frac{\partial^4 q}{\partial z^4} + (\rho_s A + \chi)\frac{\partial^2 q}{\partial t^2} = f_{body} \quad \text{(eq. 1)}$$

Here, *q(t)* is the filament displacement in the horizontal plane in direction of the horizontal flow vector at the filament location (later in the article, the displacement *Q* at the tip of the filament is measured as a vector in the horizontal plane at the surface of the canopy). The first term represents the force due to the elastic bending of the filament, whereas the second describes the inertial force of the acceleration and the third is the fluid-induced body force per unit length. By choosing proper reference values, the system leads to two non-dimensional numbers, namely, the reduced velocity *T** and the Cauchy number *Q** (Sundin and Bagheri 2019) . The first is

$$T^* = \frac{T_s}{T_f} = \frac{1}{T_f}\left(h^2\sqrt{\frac{\rho_s A + \chi}{EI}}\right) \quad \text{(eq. 2)}$$

where ρ_s is the density, A the cross-sectional area, *E* the Young's modulus and I the area moment of inertia of a filament. The constant χ represents the added mass. The numerator T_s is proportional to the period of natural free vibrations of a filament in the fluid environment, which we measured as 120 ms in the working liquid. The characteristic time of the fluid fluctuations T_f is herein the inverse of the velocity of the vortex ring divided by the diameter of the vortex ring, which calculates to 110ms. Thus, the filaments adapt to approximately the same time-scale as the flow changes. The second number represents a Cauchy number, which describes the static deformation under load:

$$Q^* = \frac{Q}{d/2} = \frac{\langle F\rangle h^3}{EI \cdot d/2} \quad \text{(eq. 3)}$$

where $\langle F\rangle$ is the acting integral force. The typical average bending *Q* of the filaments during the impact is about one-times the filament diameter *d*, therefore both *T** and *Q** are of the order of 1, indicating a strong fluid–structure interaction in the canopy. Note, that the average is taken over impact time and over the area of the vortex ring impact zone. While the average is of the order of one-times the filament diameter, peak values of the deflection for some of the filaments can reach locally around 4-5-times the filament diameter, sometimes more than the filament inter-spacing.

The sediment resuspension is commonly described in terms of the Shields parameter

$$\theta = \tau/(\rho_p - \rho)gd_P \quad \text{(eq. 4)}$$

where τ is the bed shear stress (Munro, Bethke, and Dalziel 2009). Vertical lift-off of the particles occurs when the lift force $F_L = \pi\tau d_P^2$ exceeds the particle buoyancy. We could not measure herein directly the bed shear-stress within the canopy, nevertheless the velocity field captured above the canopy surface allowed us to track the vortex core during impact. Since the canopy height in our study is of the same order as the size of the vortex core, we can expect a stronger correlation between the bed wall-shear, the strength of the vortex and how far the vortex penetrates towards the bed when impacting the canopy. We will look later in our results for possible correlations between regions of larger particle depletion, high radial velocity at the canopy surface (tangential to the tips of the forest of posts) and closest distance of the vortex core to the wall during the impact.

The measurements contain three parts as follows: firstly, the method of Time-Resolved Particle Image Velocimetry (TR-PIV) is used to obtain the flow field above the canopy. Secondly, the bending of the flexible filaments in the canopy is measured during the impact of the vortex ring by tracking their tips. Finally, the deformation of the suspension is measured by a light attenuation method, similar as described in (Bethke and Dalziel 2012). In the following, the methods are explained in more detail.

2.1 Velocity field measurements

The transparent flow chamber offers full optical access to different planes from the side and the bottom of the tank. A time-resolved PIV imaging system is used, comprised of a high-speed camera (Phantom Miro 310/311, Ametek) with CMOS sensor of 1280×800 pixels recording at 2000 frames per second, equipped with a lens (Tokima Macro f= 100 mm, F 2.8). The imaging magnification factor is M = 0.15. A continuous wave Argon-Ion laser (Raypower 5000, 5 W power at λ = 532 nm, Dantec Dynamics) holds as an illumination source. The output laser beam is about 1.5 mm in diameter and is further expanded to a sheet. For the experiments, the laser sheet is arranged in two variants: the flow field in the vertical x-z plane is recorded with the camera configuration A as shown in Fig. 1, looking from the side onto the flow in the vertical plane. For configuration B, the light-sheet is oriented in a horizontal x-y plane at a fixed height 1mm above the canopy in the fluid. Now, the camera looks from the side through a 45° mirror from the bottom of the tank in vertical upward direction through the transparent canopy onto the flow in the horizontal cross-section. As the sand particles now obstruct the optical access to the horizontal light-sheet plane above the canopy, we took these flow measurements in configuration B without any sand particle. We assume that the presence of the loosely-packed thin sand-layer at the floor of the canopy (max 3mm thickness) is of second-order influence onto the flow field of the approaching vortex-ring above the 10mm high canopy. This is because the dense forest of the 10mm high posts oppose the flow much stronger than the movable particles close to the floor. Comparative flow measurements above the canopy in the vertical plane (configuration A) without and with a 3mm thick loosely-packed sand layer at the canopy floor showed no discernible differences under the given flow conditions. Neutally buoyant particles with a nominal diameter of 30 µm are chosen as flow tracer. The data post-processing contains image pre-processing, 2D cross-correlation of successive images to calculate the vectors following an iterative grid refinement method. For the flow field data, the final interrogation window has a size of 32×32 pixels and processing is done on a grid with 50% overlap ratio. The resulting vector grid is then used to calculate the out-of-plane component of the vorticity vector. For the case of the radial measurement plane, the equidistant Cartesian velocity grid is later interpolated onto a polar-type grid with constant spacing in radial and azimuthal direction with the velocity components $v_r(r,\alpha)$ and $v_\alpha(r,\alpha)$.

2.2 Filament bending motion

The detection of the filaments' bending motion during the vortex impact is done by imaging the tip motion from the side and from below, see camera configuration A and B respectively. For the camera configuration B, the canopy is again not filled with the sand suspension with the same argument of optical access as given in section 2.1. Again, we assume that the presence of the thin sand-layer at the floor near the foot of the filament is only of second-order influence on the bending motion compared to the contribution to the tip bending due to the flow-induced load along the free end. Firstly, the particle layer at the floor is loosely-packed and free to relocate with the motion of the cantilever beam (filament) near the wall, therefore the mechanical behaviour of the cantilever beam (see eq. (1) and (3)) is basically not changed. Secondly, the bending of a one-sided clamped cantilever beam is dominated by the forces acting along the tip, while the forces near the foot contribute much less to the balance of moments, and therefore to the tip displacement. Comparative measurements of filament tip displacement from the side view (configuration A) without and with a 3mm thick loosely-packed sand layer at the canopy floor, finally, showed no discernible differences under the given flow conditions. To detect the tips, the filaments are fluorescent-labelled at the tip with a fluorescent dye containing Fluorescent Polymer Particles (PMMA-RhB-Frak-Paticles, Dantec Dynamics). The peak in the emission spectrum of the fluorescent dye is at a wavelength of 584 nm, while maximum absorption is near the wavelength of the illuminating laser light. The camera lens is equipped with a long pass filter (transmission wavelength: 560 - 1650 nm, Edmund Optics Ltd), which blocks all light from the laser and reflections from the canopy, only transmitting the light of the fluorescent-labelled tips. Thus, the tips of the filaments appear as bright dots against a black background. See Fig. 4a and 4b for a comparison of images with and without the filter. In addition, the camera configuration B is equipped with a telecentric lens (Sill Optics) which offers parallel lines of sight when capturing the tips' displacement from a bottom view. This ensures that the image has constant magnification over the depth of the telecentric range. For the tip's displacement data, each image is cross-correlated with the first reference image, i.e. the resting condition before the impact of the vortex ring. The 2D cross-correlation processing is then done in small interrogation windows around the original positions of each spot (x_i,y_i) in the reference image. This provides the tip displacement vector field in each instant of the recorded series. To display as a contour plot, the tips' displacement vectors $Q_r\left(x_{i,}y_i\right)$ are interpolated onto an equidistant Cartesian grid. Note that the tip's displacement is assumed to be proportional to the bed shear stress imposed by the radial fluid velocity component $v_r(r, \alpha)$ above the layer surface. As argued by Munro et al. (Munro, Bethke, and Dalziel 2009), the bed shear stress is expected to be maximum directly below the vortex core.

2.3 Bed surface deformation

The measurements applied herein follow the light attenuation method documented earlier by Bethke and Dalziel (Bethke and Dalziel 2012). The bed of the particles is recorded with a camera from below, through the transparent glass wall. A light source is placed above the tank, illuminating the sand layer from above. A mirrorless camera with 35mm full-frame CMOS image sensor (ILCE-7, Sony Ltd) is used to capture the intensity field. The attenuation method assumes that the intensity of the diffusively scattered light travelling through the thin bed is inverse proportional to the bed height h_p. This has been proven by testing with three different thicknesses of homogeneous particle layers, which were taken for calibration and validation of the method, see also previous applications of the method reported in (Munro, Bethke, and Dalziel 2009). The first image before any impact of a vortex ring is used as a reference when the particles are uniformly distributed and form a horizontal layer with constant thickness in the quiescent flow tank. The corresponding intensity field is denoted as $i_{n=0}(x,y)$. The experimental procedure is a follows: from the initial condition with quiescent flow we start with the first impact *n* = 1. The corresponding first snapshot image $i_{n=1}(x,y)$ is captured when all filaments are back to their original location (straight vertical) and any residual flow in the chamber has ceased to zero. Successive impacts are then studied in the same way and snapshots $i_n(x,y)$ are taken one after the other. With each shoot, the near-surface particles in the region of maximum shear stress directly below the ring core are transported, resulting in the formation of a circular mound, the radius of which increases as the vortex is stretched, see also (Munro, Bethke, and Dalziel 2009). Therefore, the intensity in the region of the mound decreases and the image gets darker there. Meanwhile, at the region of highest bed wall-shear, the particle erosion leads to increase of the intensity. We stop the experiments when we observe first signs (small empty patches) of local complete particle depletion in the evolving erosion crater, i.e. the crater has reached the floor.

In the image processing, we blank the circular areas at the filament foot positions and use only the regions between the straight filaments for data processing. The non-dimensional intensity field is calculated for each shoot as $I_n(x,y) = [i_0(x,y) - i_n(x,y)]/i_0(x,y)$ and transferred with the calibration function into a surface deformation $\Delta h_{P,n}(x,y)$ of the bed. The uncertainty of the given values in Δh_p is $\pm$ 0.1mm, which is obtained from the calibration procedure. We define herein σ_n as an accumulated resuspension value, which is calculated as the standard deviation of $\Delta h_{P,n}(x,y)$, equivalent to the RMS roughness of the deformed surface. Therefore it takes into account not only particle depletion but also re-deposition in the impact region, both contributing to the surface deformation.

For comparison, we take the flexible case as a reference. N_{flex} is the number of impacts until the eroded crater reaches the floor. The measured resuspension value at this stage is used as a reference for the rigid case and we look in the data how many impacts N_{rigid} were needed to reach the same level of resuspension. These data are then collected in a table to illustrate the difference of the configurations tested. Quantitative data are shown as normalized values, plotting the normalized resuspension $\overline{\sigma_n} = \sigma_n/\sigma_{N_{flex}}$ over the normalized impact number defined as $\bar{n}$ = n/N_{flex}.

2.4 Bed and Canopy configurations

A series of configurations with different particle bed height h_P, filament stiffness and arrangement are investigated as shown in Table 1. A pair of cases with the same bed height but different filament flexibility such as Case RH20 and Case FH20 works as a comparison pair. The table provides also the total impact times *N* until first empty patches occur in the sediment at the valley of the crater. The results show that *N* is always smaller for the flexible filaments configuration compared to the rigid ones.

Table 1. Geometric and dynamic properties of the configurations that are investigated.

Case	Filament traits	Filament arrangement	h_p (mm)	h (mm)	h_p/h	N
RH10	Rigid	Hexagonal	1	10	0.1	10
FH10	Flexible	Hexagonal	1	10	0.1	8
RH20	Rigid	Hexagonal	2	10	0.2	32
FH20	Flexible	Hexagonal	2	10	0.2	24
RH30	Rigid	Hexagonal	3	10	0.3	62
FH30	Flexible	Hexagonal	3	10	0.3	44
RR30	Rigid	Random	3	10	0.3	104
FR30	Flexible	Random	3	10	0.3	80
SH	Rigid	Hexagonal	3	3	1	17
FW	Flat wall	-	3	-	-	4

3. Results

The flow evolution above the canopy is shown in Fig. 3 for the flexible filaments configuration. The left column presents the vertical flow field while the right column displays the corresponding radial flow evolution at the horizontal interface between the main flow and canopy layer. The initial phase of approach and first contact with the canopy layer occurs at *T*=-1. Then the primary vortex ring expands to a radius of ∼0.6*D* at *T*=1 when impacting and thereafter slightly expands further over *1.9T* time period. As the vortex approaches the canopy it generates a strong radial velocity parallel to the canopy surface below the core, induced by the tangential velocity at the edge of the vortex core $\Gamma_0/(\pi R_c)$. The location of peak radial velocity occurs directly below the vortex core and shifts from *r*/*D*∼0.45 at the first contact to *r*/*D*∼0.6 when impacting, and further to *r*/*D*∼0.65 at *T*=2.9. The tangential velocity as well as the core vorticity decrease during the penetration into the canopy layer, indicating the effect of dissipation imposed by the posts within the porous layer.

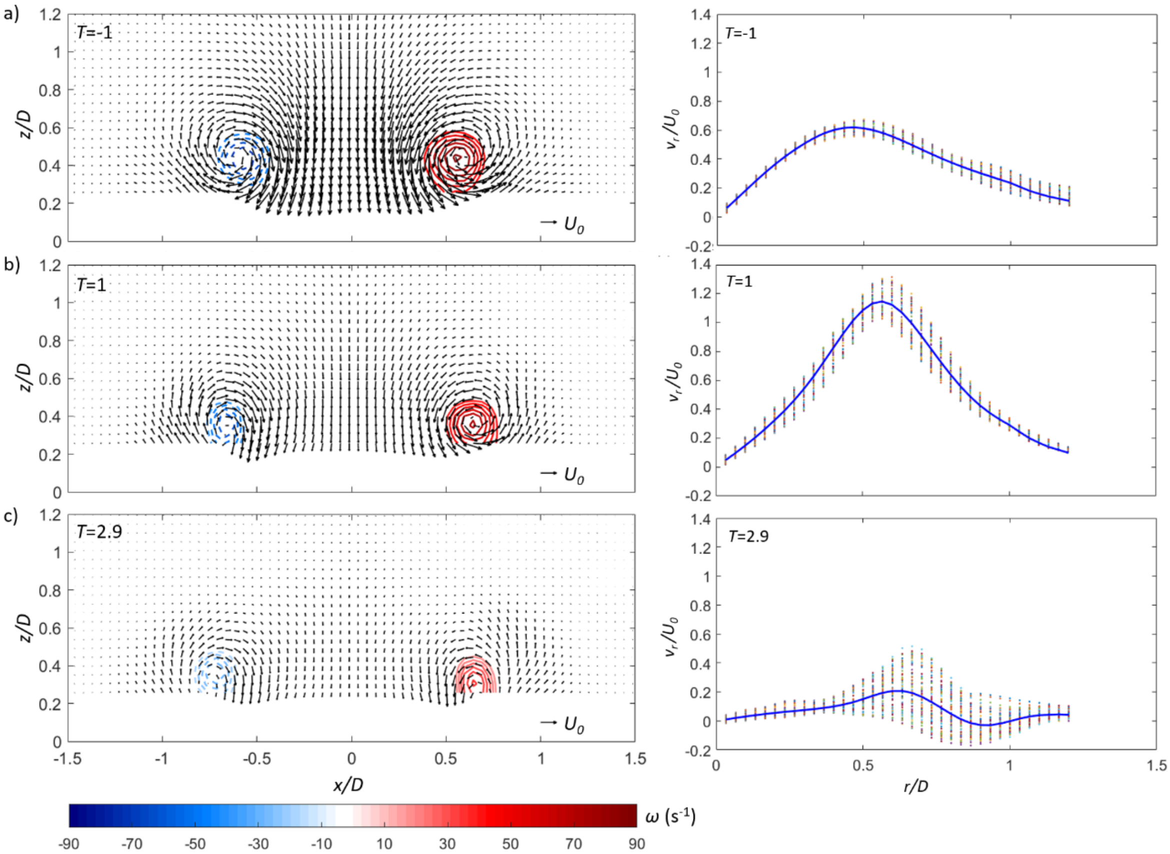

Fig. 3. Velocity field in the vertical plane overlaid with vorticity contours are shown in the left column. The right column displays the mean of the radial velocity (averaged over the circumference) plotted over the radius in the horizontal plane 1mm above the canopy (blue solid line). The colored dots illustrate the variation of $v_r(r, \alpha)$ over the circumference.

Fig. 4 shows the track of the centre of the primary vortex core over time for the different canopy configurations (flat wall, 10mm rigid canopy, 10mm flexible canopy), plotted as the wall-normal distance over time. This is derived from the cross-sectional vorticity field in each time-step by searching for the peak location in the vorticity field, see Fig. 3. The data at the maximum are fitted with a 3-point 1-D Gaussian fit in both x- and z-diretion to achieve higher precision. The major outcome for the canopy with flexible filaments is that the vortex core during impact gets closer towards the wall than for the rigid one before it rebounds again.

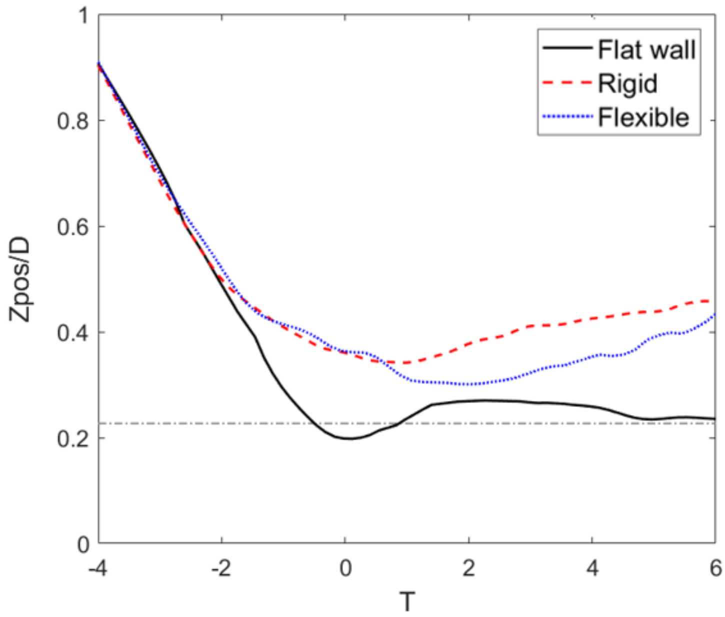

Fig. 4. History of the wall-normal distance of the vortex core position during the impact of the vortex ring in the vertical centre plane (*x-z* plane). The grey dash-dot line denoted the location of the surface of the canopy relative to the flat wall.

Fig. 5 illustrates exemplary the deflection of the flexible filaments along one row through the centre for *T*=1. As seen by the strong deflection of the tips, the surface can quickly comply with the vortex impact, opening up its interface. Thus it allows the core to penetrate further towards the bed as in the case of the rigid canopy, see Fig. 4. For mechanical reasons, strong lateral bending of the filaments also leads to a considerable lowering of the tip in vertical direction, effectively seen by the indentation of the interface, most pregnant at time *T=1* in regions of maximum lateral bending at about *x*/*D*~0.5-0.6. Comparing the flow field at the same time *T=1*, this region is at the radial position where the vortex core penetrates into the canopy and where the maximum radial velocity is oberved at the interface, see Fig. 3. The effective height of the canopy is there reduced down to *h**=85% *h*. As the size of the vortex core is similar to the canopy height in our study, we expect an increase of the bed wall-shear the deeper the vortex can indent the interface and penetrate towards the bed. We will look later in our results for a possible correlation between regions of larger particle depletion and filament bending (interface indentation).

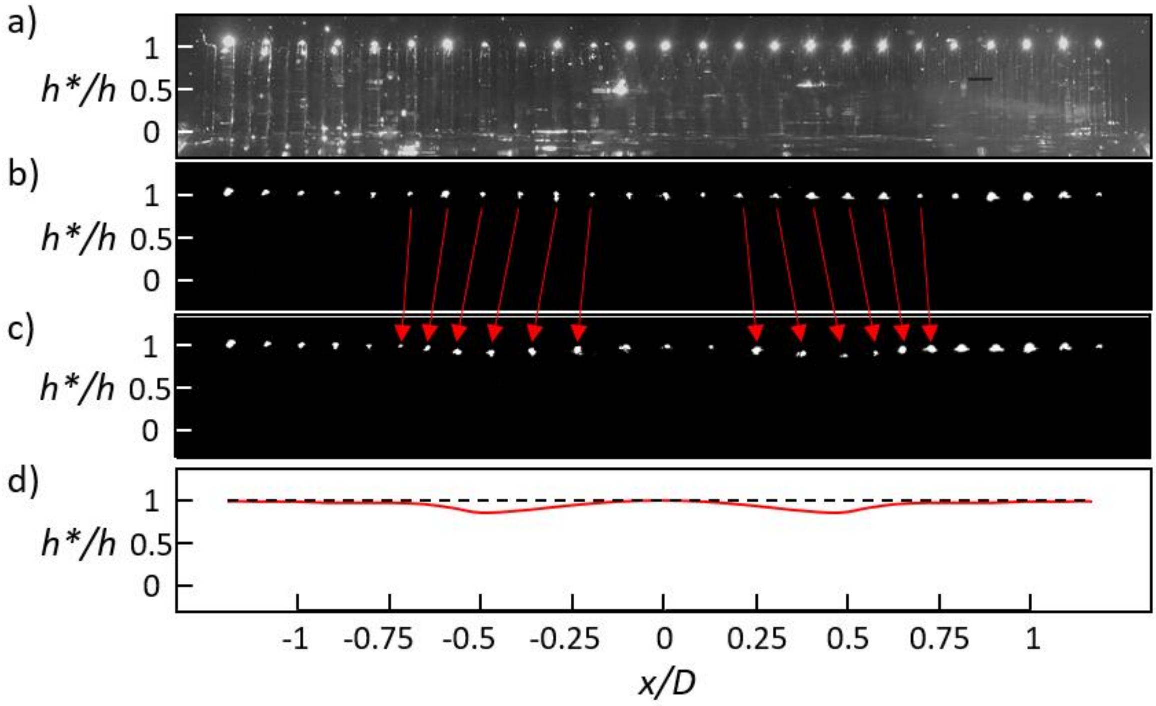

Fig. 5. a) Image of a row of flexible filaments in the vertical *x-z* plane before vortex ring impact. When putting the long pass filter on, the reflections along the filaments are filtered out and only the tips appear as the bright spots in b). Impacting of the vortex ring on the canopy layer cause the bending of the flexible canopy, the tips' displacement of which are shown in c). d) The plot of the effective height h^* profile of the flexible canopy interface (denoted by the red solid line), compared with reference height h before the impact (denoted by the black dash line).

Fig. 6 displays the bottom view of the tip locations before (T=-∞) and after the impact at T=1 by Image A and Image B separately. By overlaying Image B on Image A, we obtain a combination image showing the tip displacement vectors $Q_r(xi,yi)$ in the hexagonal pattern. Also, from the zoom-in view, one can see that maximum tip displacement can reach the distance of the inter-spacing between neighbouring filaments.

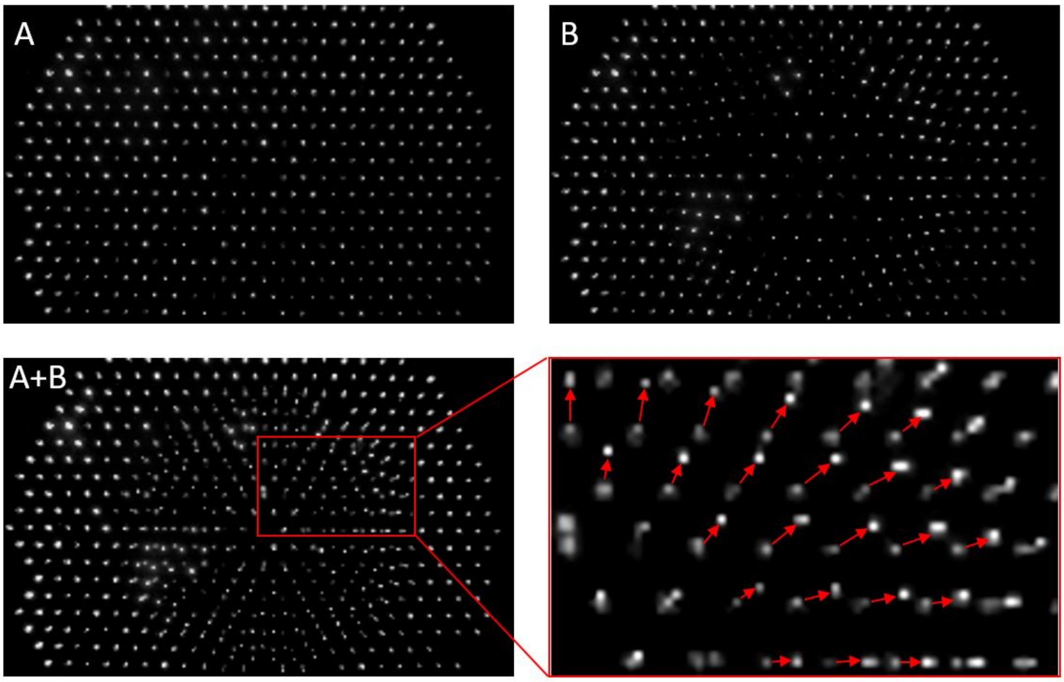

Fig. 6. Images of filament tips before the impact of the vortex ring (image A, $T = -\infty$) and at the impact (image B, T=1). The combination (image A+B) of image A and B shows the displacement of the tips, with denoted by red arrows in a zoom-in view.

Since the vectors are pointing approximately radially outwards from the centre of the canopy (the axis of the impacting vortex ring), the dominant component of $Q_r(x,y,T)$ is the radial component. Further information is obtained from contour plots of $Q_r(x,y,T)$ over several time steps, see Fig. 7.

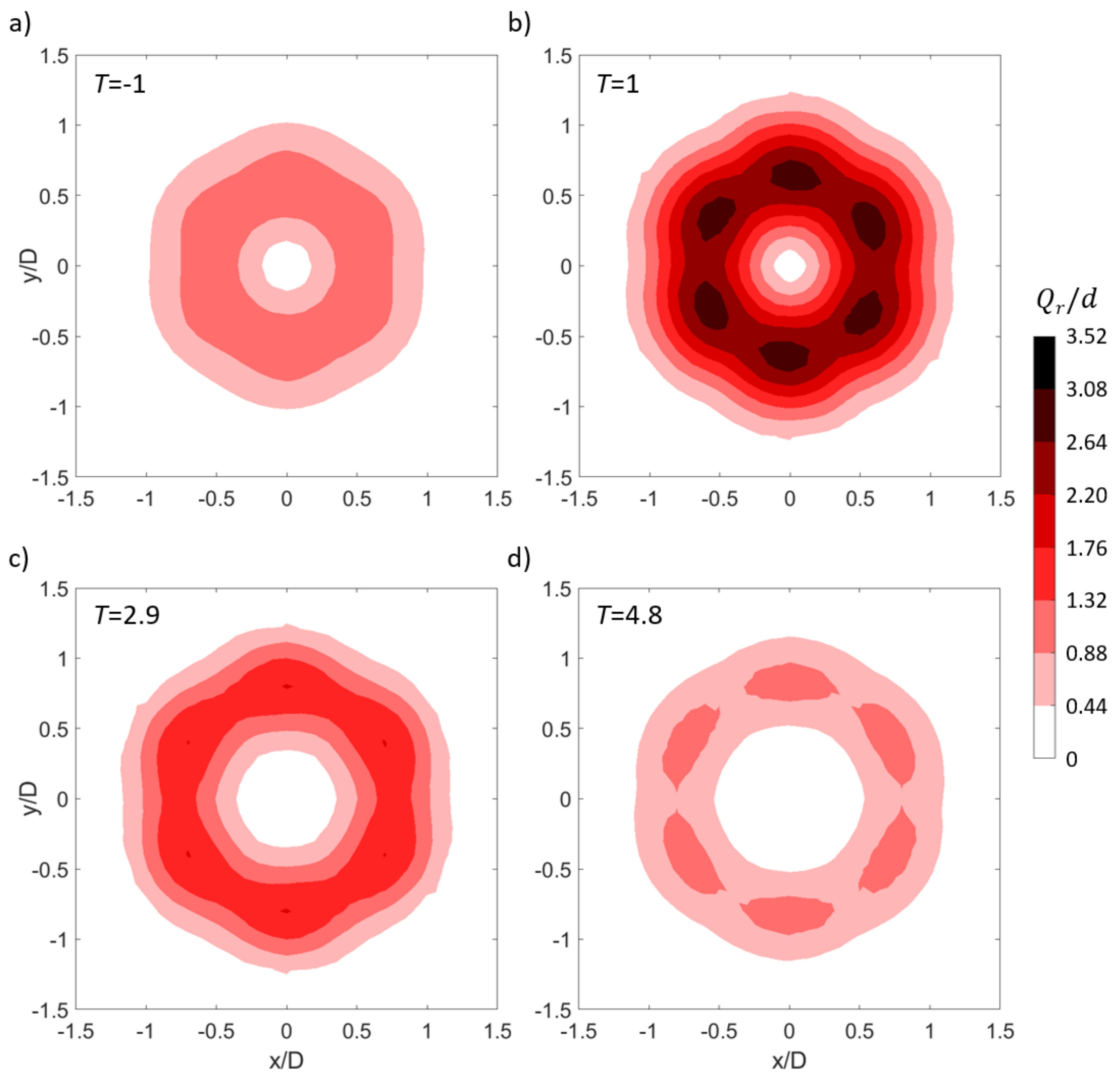

Fig. 7. Evolution of the contours of the tip displacement for flexible filaments configuration at a) *T*=-1, b) *T*=1, c) *T*=2.9 and d) *T*=4.8. The tip's displacement $Q_r(x,y,T)$ is normalised by the filament diameter *d*.

The contours of the displacement field are not perfect axisymmetric but show a footprint of the hexagonal structure of the canopy. Previous studies in our lab haven proven that the vortex ring deforms into a hexagonal pattern after impact due to a lock-in effect of the azimuthal instability with the hexagonal grid (Li and Bruecker 2018). Interestingly, the peak values of Q_r occur not along the preferential pathways along $\alpha = 0° + j * 60°\ (j = 1,2,3 \dots)$ but in between at angles of $\alpha = 30° + j * 60°\ (j = 1,2,3 \dots)$. The average radius of maximum radial tip displacement is at about 0.5-0.6 *D* at the beginning of impact and it expands to 0.8*D* at the late phase when peak values of bending decrease down to the order of 1*d*.

When repeating the experiments with the sand-layer inside the canopy we see the evolution of a similar hexagonal pattern of the deformed sediment. A comparison of the typical distribution after n = 44 shoots for the rigid and the flexible canopy is illustrated in Fig. 8.

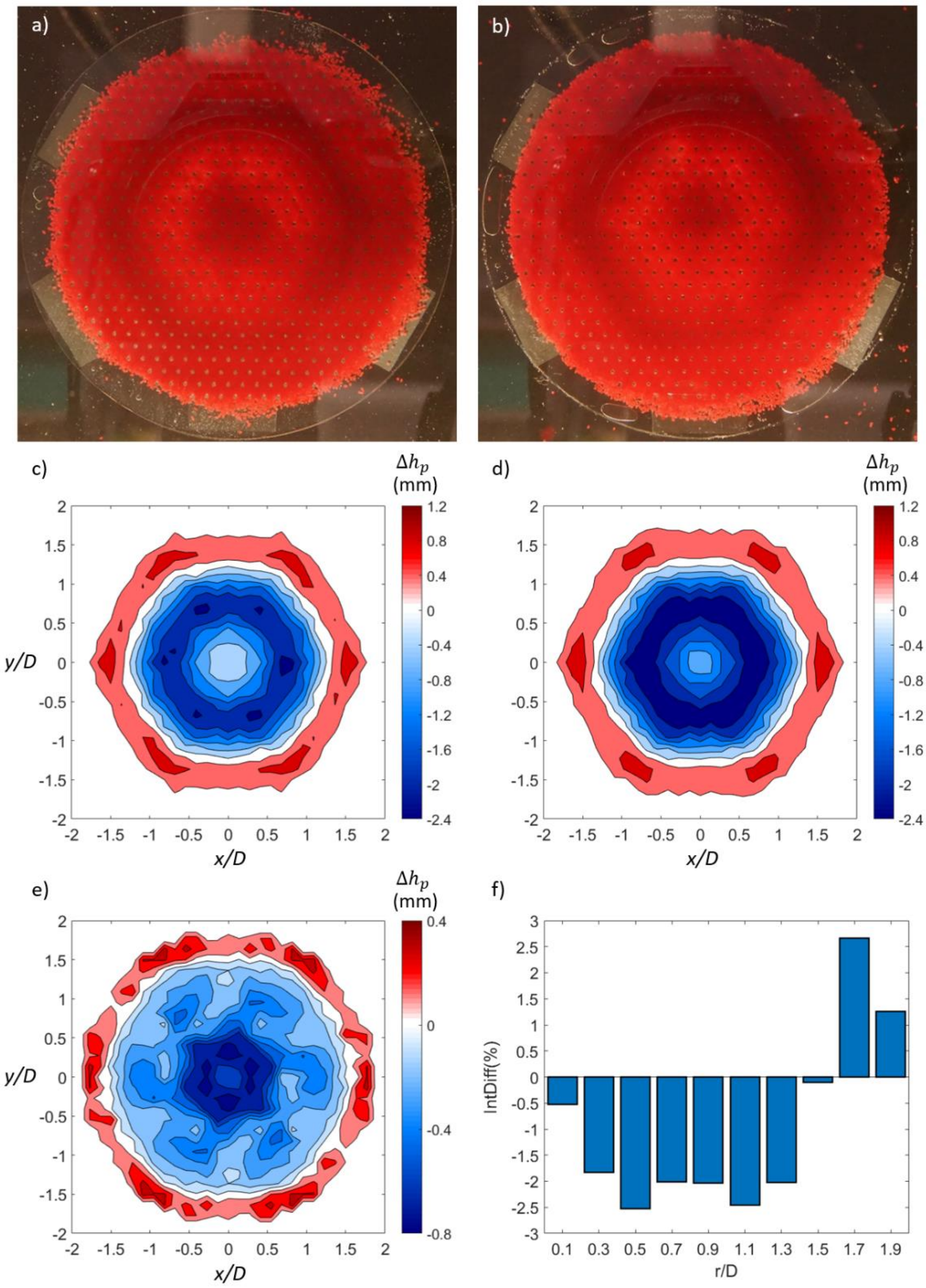

Fig. 8. Images showing the crater pattern eroded by the impact of vortex ring after n=44 times of impact for case RH30 a) and FH30 b). Corresponding contours of the bed surface deformation in mm are shown in c) and d). e) Contour plot of difference in local bed surface height between FH30 and RH30; f) bar chart of the difference in percentage of the total bed volume within the impact region (r

≤ *1.3D)*. The values are obtained by integrating the contours in e) over different circular ring areas of Δr=0.2D ($\sim 2\Delta s$).

Similar as observed in (Munro, Bethke, and Dalziel 2009) for a single shoot experiment on a flat wall, we observe after several shoots the slow formation of a crater. Maximum particle depletion occurs at a radius of $r/D \sim 0.6$ (ring of dark blue), just in the region below the vortex core where the radial velocity at the interface of the canopy is maximum. On the other hand, particles are accumulated in a ring at a larger diameter $r/D \sim 1.5$, building the crest of the crater. Furthermore, we also see a small mound of uneroded particles remaining at the crater centre below the axial stagnation point of the vortex ring. These results demonstrate that the ring-like region of maximum particle depletion (at $r/D \sim 0.6$) agrees with the location of peak radial velocity at the surface of the canopy during the impact in Fig. 3b, therefore regions of elevated levels of bed wall-shear are seemingly correlated with regions of high radial velocity at the canopy surface.

As a striking feature of our experiment, the crater is not perfect circular but shows a hexagonal pattern of the crest, orientated in the same way as the hexagonal pattern of the canopy (see (Li and Bruecker 2018)). The local maxima along the crest of the crater are aligned with the orientation of the preferential pathways in the canopy. Comparing the results for the flexible case FH30 with the rigid one RH30 shows that the diameter of the hexagonal crest is a bit larger, in addition the magnitude of particle depletion in the crater is more pronounced. The difference between the bed surface levels of FH30 and RH30 is included as a subplot in Fig. 8e. For further clarification, we show in Fig. 8f the percentage of bed volume which the flexible case is able to further resuspend compared to the rigid one. The values, integrated along different circular ring diameters, show that more particles have eroded from the crater valley region and relocated at the outer crater crest than for the rigid case. What can be seen is a surplus of about 13% of bed volume more removed from the crater, and 4% more added to the growth of the crest. This demonstrates that flexibility of the posts has promoted particle resuspension under otherwise identical initial and boundary conditions. Note, that surface levels at *r* > *1.9D* are not captured in the image processing and particles may have left their original region completely, therefore the percentages in Fig. 8f in sum do not necessary cancel out to zero. Rather, it shows that there is also a surplus in net radial outflux of the bed volume at the canopy border for the flexible case, which is about 9% higher.

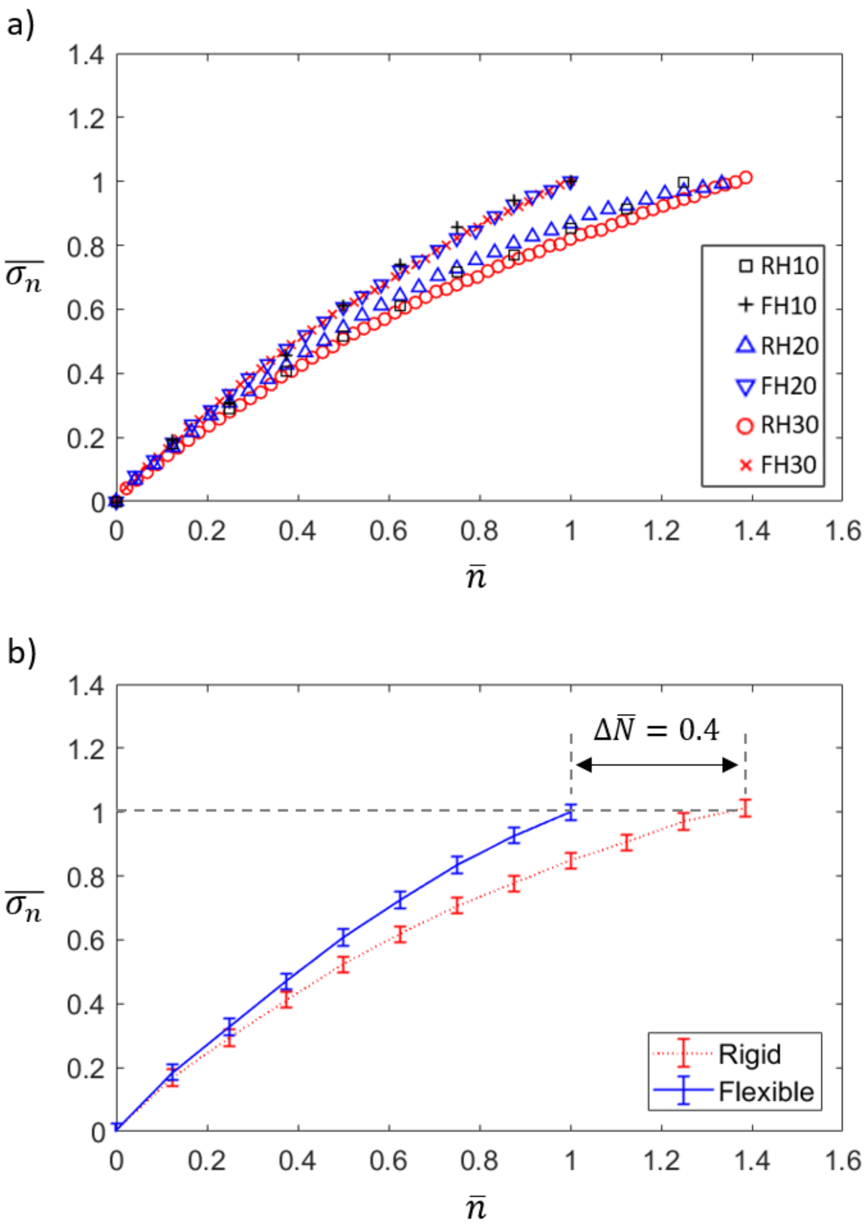

Fig. 9. a) Plots of the accumulated effective resuspension $\overline{\sigma_n}$ over the amount of impacts of the vortex ring for rigid canopy and flexible canopy for three sets of bed thicknesses. The details of configurations are listed in Table 1. For each comparison pair, the effective resuspension is normalised by $\sigma_{N_{flex}}$ of the flexible filaments configuration. $\bar{n}$ is the normalized number of impacts, defined as impact number *n* divided by the total number of impacts N_{flex} of the flexible filaments configuration. b) Plots of mean normalized resuspension of rigid canopy and flexible canopy respectively with error bars.

We further plot the history of the accumulated resuspension σ_n over increasing number of shoots for all experiments in a single diagram, see Fig. 9. When we initially did that, we saw that the profiles look self-similar. Therefore, we show the profiles in a normalized form by plotting $\overline{\sigma_n} = \sigma_n/\sigma_{N_{flex}}$ over the impact number $\bar{n} = n/N_{flex}$ (recall that the characteristic impact number *N* for the flexible canopy is always less than that for the rigid canopy). Firstly, the normalization shows that the profiles for the flexible cases collapse into approximately one single curve for all different bed thicknesses. The same holds for the experiments with the rigid canopies, though the scatter is somewhat larger. Secondly, plotting the average for the different bed thicknesses together with the error-bars illustrates that the scatter is well within the range of the measurement uncertainty, therefore the observed behaviour clearly demonstrates a physical reason for the different trends in both curves. They show for the same values of $\overline{\sigma_n}$ constantly an approximately 20% higher accumulated effective resuspension for the flexible canopy. Alternatively, one can interpret the data along the horizontal axis. We observe for the rigid canopy about 40% lower resuspension rate (accumulated resuspension per impacts), highlighted by $\Delta\overline{N}$ = 0.4 at $\overline{\sigma_n}$ = 1 in Fig. 9b.

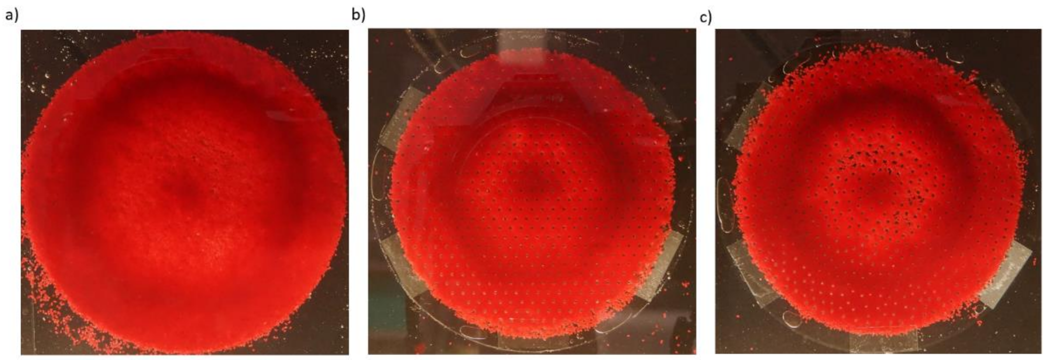

Fig. 10. Images showing the crater pattern eroded by the impact of the vortex ring in configuration of particle layer thickness h_p =*0.3h* for a) flat wall after *N* = 4 impacts, b) FH30 after *N* = 44 impacts and c) FR30 after *N* = 80 impacts.

Finally, a comparison of the intensity field for the random arrangement in Fig. 10 proves that the hexagonal pattern of the crater in Fig. 8 is indeed a consequence of the underlying canopy structure. With a random arrangement of the posts in the forest, the crater approaches a rather circular shape. However, the necessary number of successive shoots to reach the same effective resuspension has increased about a factor of two, see Tab. 1. Nevertheless, the flexible canopy again reaches this state much earlier as seen from Tab. 1.

4 Discussion

Comparing the resuspension of particles in a canopy of the same geometry with rigid posts and flexible posts of the same shape concludes that flexibility of the posts has improved resuspension. What can be seen is a surplus of about 13% of bed volume more removed from the crater in the region $0.5 \leq \mathrm{r}/D \leq 1.1$, which agrees with the region of considerable tip displacement of the filaments radially outwards with values of $Q \geq 1d$ during the impact of the vortex ring. At the inner part of this region in $0.5 \leq \mathrm{r}/D \leq 0.8$ is where a) the strongest indentation of the canopy surface is observed, b) maximum radial velocities at the interface are observed and c) the vortex core penetrates closer towards the bed. Under the given conditions of canopy height equal to the vortex-core size and the given canopy properties (filament size, spacing, Cauchy-number), these results prove the strong correlation between locations of peak bed shear-stress (maximum of particle depletion), peak radial velocity at the interface to the canopy and peak indentation. Based on these results we propose a conceptional model for the given situation, which assumes in first approximation that the bed wall-shear is proportional to the strength Γ_0 of the impacting vortex and inversely proportional to the canopy height *h**, see Fig. 11 and eq. (5) with ν as the kinematic viscosity of the fluid.

$$\tau \approx \nu\rho \frac{\Gamma_0/(\pi R_c)}{h^*} \qquad \text{(eq. 5)}$$

The expression of the vortex strength in form of $\Gamma_0/(\pi R_c)$ describes the radial velocity at the interface when the edge of the vortex core reaches the canopy, which was measured in our experiments. In addition, the height *h** indicating the indentation of the penetrating vortex was measured optically, too. Following the hypothesis given in eq. (5) one can compare the curves of effective resuspension between the rigid canopy and the flexible canopy in Fig. 9 if one takes into account the effect of the indentation of the canopy (the strength of the vortex is unchanged). Recall, the effective height shows a typical value *h**=85%*h* at maximum canopy indentation, which is radially moving over the course of impact form r/D~0.5 to r/D~0.8. Therefore, following eq. (5) the wall-shear stress acting on the bed at this location is about 17% higher than in the rigid case. When applying this correction to the flexible case (reducing the $\overline{\sigma_n}$ values about 17%), both curves of effective resuspension in Fig. 9b can get to near overlap. The so achieved overlap supports the conceptional model and the assumption in eq. (5), although the exact functional description therein is not known yet. As in a porous medium the velocity exponentially reaches a Darcy flow (e.g. Brinkman layer), more accurate estimation is only possible with direct measurements inside the canopy. However, it is reasonable to argue in our case that the bending of the pillars increases locally the permeability of the bed, allowing fluid to more easily penetrate, which in turn increases shear stress. Sundin and Begheri (Sundin and Bagheri 2019) concluded, that such surfaces with soft filaments in turbulent channel flow increase the entrainment of free fluid into the bed and may be useful in application where mixing and entrainment are beneficial. The present results confirm the enhanced mixing in the flexible canopy.

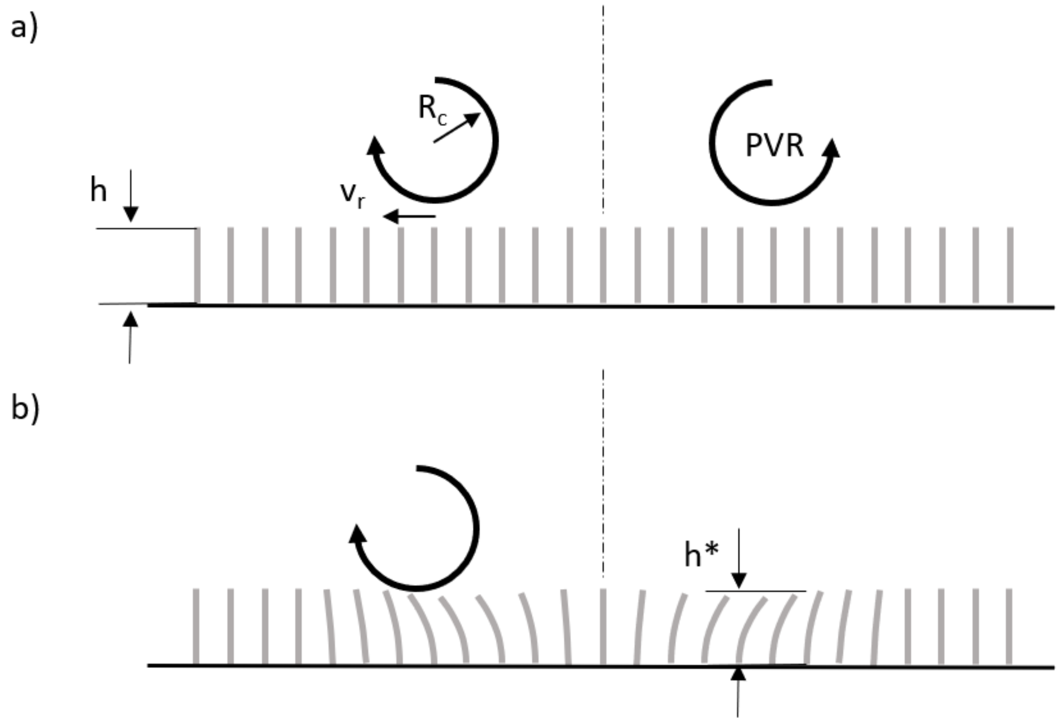

Fig. 11. Conceptional model of the impacting of the vortex ring on the compliant canopy layer: a) the primary vortex ring (PRV) with the core radius R_c approaches the tips of the canopy layer. The vorticity induces a strong radial outwards-direct velocity component v_r at the interface underneath the vortex core, inducing locally strong filament bending. b) the indentation of the interface effectively reduces the height of the canopy layer h^* and allows the vortex core to penetrate deeper towards the bed floor.

The crater measurements herein show in general many similarities to the results obtained in single shots of vortex rings on sand-layers on a smooth flat wall (Munro, Bethke, and Dalziel 2009). With the underlying canopy structure, it requires much more shoots to achieve considerable resuspension due to the resistance within the canopy layer, however the global pattern resembles those with a single shoot in a plane wall. If the canopy has preferential pathways due to anisotropic arrangements of the posts or other structural elements, the overall performance of resuspension improves and the crest of the crater deforms accordingly. A proof is given by recovering a hexagonal structure of the crest of the crater after several shoots when the underlying grid of posts has a hexagonal arrangement. Interestingly, if a canopy of the same porosity is studied with a random arrangement of the posts, the effective resuspension is largely reduced. This is probably because of the tortuosity of the particle paths while moving through the forest of posts and the non-linear characteristics of bed resistance in local unit-cells of posts with different mean porosity. It is assumed that particles remain much longer trapped in regions of posts with high local density than they are free to move in sparser regions.

5. Conclusions

The following conclusions are based on the above described laboratory experiment under well defined and ideal conditions of the impact of an axisymmetric laminar vortex ring on the canopies. Most importantly, the height of the canopy here corresponds to the size of the vortex core. This is not directly transferable to the situation of turbulent flows over natural canopies, but it's being investigated here as a benchmark experiment to understand the interaction of vortical flows with poroelastic layers such as filamentous walls, the necessity of which was recently emphasized in the review of Bottaro (Bottaro 2019) for the purpose of near-wall control of turbulent boundary layer flows using engineered poroelastic coatings. The results for the filamentous canopies studied herein (see Tab. 1) have shown three major aspects of the vortex-impact induced resuspension:

- Flexibility of the posts increases the efficient resuspension by the amount it allows the indentation of the compliant interface (reducing the effective canopy-height) due to the bending of the flexible structures. Scaling of the results with the effective canopy height leads to a collapse of the curves for the observed resuspension in the history of several successive impacts when comparing the rigid with the flexible canopy. This result should be independent of the arrangement of the filaments in the canopy. It is interesting to further investigate if the observed effect can be predicted alternatively by an effective increase of the local permeability of the flexible canopy where filaments bend away from each other (the pore-size opens up locally). This can be tested assuming roughly that permeability scales with pore-size squared, exact relations can be found in (Sangani and Acrivos 1982).

- The pattern of resuspension of an initially homogeneous sand-layer in the canopy is determined by the local structure of the canopy. In the experiment with a hexagonal arrangement, the preferred pathways in this anisotropic (poroelastic) layer change the transport paths of the particles. Although the head-on impacting vortex is initially a symmetric structure, the observed crater pattern transforms quickly into a hexagonal shape. Stronger transport is observed along the preferential pathways where the filament bends less than in the directions of higher canopy resistance. Note that the impacting vortex ring generates a pattern of six radial jets which are aligned with the preferential pathways in the hexagonal pattern, as shown in our previous study (Li and Bruecker 2018).

- Comparing a layer with randomly arranged filaments with the hexagonal structure at the same average porosity show a dramatic decrease of the overall average resuspension efficiency. It needs roughly double amount of impacts to obtain the same amount of particle redistribution on average in the impact region. This proves that the preferential pathways in the canopy play a large role in resuspension. The random path of the particles around the filaments is affected in a non-linear manner by the local resistance. Regions of locally sparse arrangements of the filaments cannot balance the trapping effect of particles within regions of dense arrangement in their travel history. Nevertheless, flexibility helps again to improve resuspensions, similar as observed in the hexagonal arrangement.

Restrictions in the choice of material for the filaments to obtain full transparency of the canopy and the associated special manufacturing conditions have so far not enabled us to examine a larger parameter space. Nevertheless, the results point to the fact that measurements of the local effective height of the canopy layer may be useful to include into models for particle transport in canopies as the data overlap when scaled with the effective height of the canopy layer as the characteristic reference scale. In addition, statistical measurements of the effective canopy layer height in turbulent flow over flexible canopies could be helpful to find correlations to local differences in erosion processes.

Acknowledgment

Prof. Bruecker holds the BAE SYSTEMS Sir Richard Olver Chair in Aeronautical Engineering and the Royal Academy of Engineering Research Chair in Nature-inspired flow sensing and manipulation. The position is co-sponsored by BAE SYSTEMS and the Royal Academy of Engineering, which is gratefully acknowledged herein. The position of MSc Qianhui Li was supported by the German Research Foundation in the grant DFG 1494/32-1 which is also gratefully acknowledged. We thank Prof. Uwe Schnakenberg from IWE1, RWTH Aachen, Germany, for support in building the transparent canopies.

References

Bandyopadhyay, PR, and R Balasubramanian. 1995. "Vortex Reynolds number in turbulent boundary layers." *Theoretical and Computational Fluid Dynamics* no. 7 (2):101-117.

Bethke, Nastja, and Stuart B Dalziel. 2012. "Resuspension onset and crater erosion by a vortex ring interacting with a particle layer." *Physics of Fluids* no. 24 (6):063301.

Bottaro, Alessandro. 2019. "Flow over natural or engineered surfaces: an adjoint homogenization perspective." *Journal of Fluid Mechanics* no. 877.

Brücker, Ch. 2011. "Interaction of flexible surface hairs with near-wall turbulence." *Journal of Physics: Condensed Matter* no. 23 (18):184120.

Brücker, Ch, D Bauer, and H Chaves. 2007. "Dynamic response of micro-pillar sensors measuring fluctuating wall-shear-stress." *Experiments in fluids* no. 42 (5):737-749.

De Langre, Emmanuel. 2008. "Effects of wind on plants." *Annu. Rev. Fluid Mech.* no. 40:141-168.

Dewenter, Jana, Peggy Gerullis, Alexander Hecker, and Stefan Schuster. 2017. "Archerfish use their shooting technique to produce adaptive underwater jets." *Journal of Experimental Biology* no. 220 (6):1019-1025.

Li, Qianhui, and Christoph H Bruecker. 2018. "Vortex interaction with a rough wall formed by a hexagonal lattice of posts." *Physics of Fluids* no. 30 (5):054107.

Munro, Richard J, N Bethke, and SB Dalziel. 2009. "Sediment resuspension and erosion by vortex rings." *Physics of Fluids* no. 21 (4):046601.

Nepf, Heidi M. 2012. "Flow and transport in regions with aquatic vegetation." *Annual review of fluid mechanics* no. 44:123-142.

Ouriemi, Malika, Pascale Aussillous, Marc Medale, Yannick Peysson, and Élisabeth Guazzelli. 2007. "Determination of the critical Shields number for particle erosion in laminar flow." *Physics of Fluids* no. 19 (6):061706.

Sangani, Ashok Shantilal, and A Acrivos. 1982. "Slow flow past periodic arrays of cylinders with application to heat transfer." *International journal of Multiphase flow* no. 8 (3):193-206.

Schmitz, GJ, Ch Brücker, and P Jacobs. 2005. "Manufacture of high-aspect-ratio micro-hair sensor arrays." *Journal of micromechanics and microengineering* no. 15 (10):1904.

Sundin, Johan, and Shervin Bagheri. 2019. "Interaction between hairy surfaces and turbulence for different surface time scales." *Journal of Fluid Mechanics* no. 861:556-584.

Sutherland, Alex J. 1967. "Proposed mechanism for sediment entrainment by turbulent flows." *Journal of Geophysical Research* no. 72 (24):6183-6194.